nature COMMUNICATIONS

ARTICLE

Received 13 Oct 2014 | Accepted 16 Dec 2014 | Published 2 Feb 2015

DOI: 10.1038/ncomms7150

Ultrasensitive and label-free molecular-level detection enabled by light phase control in magnetoplasmonic nanoantennas

Nicolò Maccaferri[1], Keith E. Gregorczyk[1], Thales V.A.G. de Oliveira[1], Mikko Kataja[2], Sebastiaan van Dijken[2], Zhaleh Pirzadeh[3], Alexandre Dmitriev[3], Johan Åkerman[4,5], Mato Knez[1,6] & Paolo Vavassori[1,6]

Systems allowing label-free molecular detection are expected to have enormous impact on biochemical sciences. Research focuses on materials and technologies based on exploiting localized surface plasmon resonances in metallic nanostructures. The reason for this focused attention is their suitability for single-molecule sensing, arising from intrinsically nanoscopic sensing volume and the high sensitivity to the local environment. Here we propose an alternative route, which enables radically improved sensitivity compared with recently reported plasmon-based sensors. Such high sensitivity is achieved by exploiting the control of the phase of light in magnetoplasmonic nanoantennas. We demonstrate a manifold improvement of refractometric sensing figure-of-merit. Most remarkably, we show a raw surface sensitivity (that is, without applying fitting procedures) of two orders of magnitude higher than the current values reported for nanoplasmonic sensors. Such sensitivity corresponds to a mass of $\sim$0.8 ag per nanoantenna of polyamide-6.6 ($n = 1.51$), which is representative for a large variety of polymers, peptides and proteins.

[1] CIC nanoGUNE, 20018 Donostia-San Sebastián, Spain. [2] NanoSpin, Department of Applied Physics, Aalto University School of Science, 00076 Aalto, Finland. [3] Department of Applied Physics, Chalmers University of Technology, 41296 Gothenburg, Sweden. [4] Materials Physics, KTH Royal Institute of Technology, Electrum 229, 16440 Kista, Sweden. [5] Department of Physics, University of Gothenburg, 41296 Gothenburg, Sweden. [6] IKERBASQUE, Basque Foundation for Science, 48011 Bilbao, Spain. Correspondence and requests for materials should be addressed to P.V. (email: p.vavassori@nanogune.eu).

The most prominent routes for high-sensitivity and label-free detection in a compact device setting presently rely on localized surface plasmon resonance (LPR)-based technologies. The greatly enhanced electromagnetic fields at the surface of a resonant plasmonic nanostructure[1,2] allow for probing minute changes in the surrounding environment. Owing to the evanescent nature of the fields, the sensing volume of plasmonic nanostructures is only marginally larger than the structures themselves, making them ideal probes for localized changes in a medium. For these reasons, the utilization of LPRs for label-free molecular detection is under very active investigation for biochemical and biomedical applications[3–12]. They feature optical interrogation schemes, small footprint, high sensitivity of refractometric detection, potentially down to a single-molecule level because of the electromagnetic field enhancement at the nanoscale[3,4], and easy integration with a wide range of fluidic systems for analyte delivery.

To quantify the sensing performance of a LPR-based sensor, the bulk refractive index sensitivity $S_{RI} = \Delta\lambda^*/\Delta n$ is often considered, where $\Delta\lambda^*$ is the shift of the LPR peak position λ^* in nanometres measured in the extinction spectra over the change in the environment refractive index Δn. For detection at the molecular level, sensitivity to local variation of the index of refraction is most relevant. In this case sensor performances are quantified in terms of surface sensitivity $S_{Surf} = \Delta\lambda^*/\Delta t$ at a given refractive index n, where t is the thickness of an assembled thin layer of the material with refractive index n being sensed on top of the active surface. Since the final accuracy of the peak tracking depends both on the magnitude of the peak shift and on the resonance line-width, the most crucial performance-defining parameter is the figure-of-merit (FoM), obtained by dividing either S_{RI} or S_{Surf} by the full width at half maximum (FWHM) of the resonance. Current LPR-based sensors have a surface FoM lower or at most comparable to that of propagating surface plasmon resonance (SPR)-based sensors[13–15], which are the core and reference systems for label-free optical detection. However, SPR-based sensors are not an alternative for single-molecule level detection because of the lack of local sensitivity to the index of refraction. Therefore, tremendous research efforts aimed at improving the FoM of LPR-based sensors have been conducted[9,10,12,16–18].

Here we unveil a sensing modality that utilizes the unique optical properties of nanostructured magnetoplasmonic nanoantennas to combine and enhance all mentioned features of plasmonic sensing. Most importantly, we demonstrate that our approach delivers a manifold improvement of surface sensitivity and orders of magnitude higher surface FoM with respect to recent values reported for plasmonic-based detectors, including SPR-based sensors[14,15,18]. The proposed approach relies on magnetoplasmonic ferromagnetic (FM) nanoantennas deposited on a transparent substrate. FM nanoantennas are known to support LPRs[19] and, once activated by an external magnetic field, they acquire an intrinsic magneto-optical (MO) activity. The key point is the selection of the FM material and nanoantennas' design in order to produce exact phase compensation in the electric field components of the otherwise elliptically polarized transmitted light at a specific wavelength λ_ε. Under this condition, a vanishing ellipticity ε (ε null-point, that is, full linear polarization) is produced at λ_ε. Our underlying strategy relies on the fact that light polarization changes can be measured precisely especially near null conditions. The determination of λ_ε provides a phase-sensitive identification of the nanoantennas' LPR position and enables tracking of the spectral shift caused by local refractive index variations with unprecedented precision.

Results

Theoretical background. In ferromagnetic bulk materials and continuous films, the MO activity is governed by the spin–orbit interaction, which is a property intrinsic to a given material. Conversely, the MO response of a magnetic nanoantenna is governed also by LPRs[19–24]. As depicted in Fig. 1, light interacting with a magnetic field-activated FM nanoantenna excites two coupled LPRs, one directly driven by the electric field of the incident light and the second induced orthogonally by the inherent MO activity. Desired light polarization behaviour in transmission (and/or reflection) is achievable by tuning the relative phase of these two excited LPRs by designing the nanostructures. In detail, is the LPR polarized perpendicular to the driving electric field and light propagation direction that is governing the MO response of the nanoantenna. This fundamental physical effect can be visualized as follows: the incident electric field E_x^0 induces an electric dipole along the x axis described as $p_x = \alpha_{xx}E_x^0$, where α_{xx} is the diagonal element of the polarizability tensor. The corresponding oscillation of the conduction electrons along the x axis is spin–orbit coupled with the magnetization $\mathbf{M}$ within the nanoantenna, which is aligned along the z axis by the applied magnetic field in the experimental geometry adopted here. This coupling induces an additional oscillation motion of conduction electrons, that is, a second electric dipole p_y, along the in-plane transverse y axis direction. In general, the expression for the spin–orbit induced transverse dipole can be written conveniently in terms of the off-diagonal polarizability tensor elements $\alpha_{ij} = \varepsilon_{ij}\alpha_{ii}\alpha_{jj}/(\varepsilon_0 - \varepsilon_m)^2$, where ε_{ij} and ε_0, are the off-diagonal and diagonal elements of the dielectric tensor of the given constituent material, and ε_m is the dielectric constant of the embedding medium. This expression shows that the off-diagonal elements of the polarizability tensor are proportional to the product between the diagonal components of the tensor along the two mixed directions. In the present case, the spin–orbit transversally induced dipole is given by $p_x = \alpha_{yx}E_x^0 = [\varepsilon_{yx}\alpha_{yy}\alpha_{xx}/(\varepsilon_0 - \varepsilon_m)^2]\ E_x^0$ (considering the circular shape of our nanoantennas, $\alpha_{yy} = \alpha_{xx}$, that is, the two LPRs resonate at the same wavelength, and the expression above can be simplified to $p_x = \alpha_{yx}E_x^0 = [\varepsilon_{yx}\alpha^2{}_{xx}/(\varepsilon_0 - \varepsilon_m)^2]\ E_x^0$).

Notably, the transversally induced electric dipole p_y is of second order in terms of polarizability as it depends on the product of two polarizabilites, α_{xx} and α_{yy}, while the directly induced dipole p_x depends only on α_{xx}. This difference is crucial for the present application and can be understood considering that the transverse oscillation p_y is not driven directly by E_x^0 but by the induced dipole p_x with the mediation of the spin–orbit coupling. The polarization state of the far-field radiated in the z direction, either transmitted or reflected (Faraday or Kerr geometry), can be represented by the ratio of these two in-plane and mutually orthogonal oscillating electric dipoles, namely by the complex MO polarization angle $\Theta = p_y/p_x = \varepsilon_{yx}\alpha_{xx}/(\varepsilon_0 - \varepsilon_m)^2$. This expression reveals that the polarization of the transmitted and reflected light is governed by both the intrinsic properties of the constituent material $[\alpha_M = \varepsilon_{yx}/(\varepsilon_0 - \varepsilon_m)^2]$ and by the in-plane LPR in the nanoantenna (α_{yy}, which coincides with $\alpha_{xx}$for circular nanoantennas). In detail, the transmitted and reflected light will have an elliptical polarization described through measurable rotation and ellipticity angles given by $\theta = \mathrm{Re}(\Theta)$ and $\varepsilon = \mathrm{Im}(\Theta)$, respectively. Physically, both θ and ε at any light wavelength are determined by the relative phase $\Delta\Phi$ of the two scattering electric dipoles p_x and p_y, since the complex MO angle $\Theta \propto e^{i\Delta\Phi}$, where $\Delta\Phi = \Phi[\alpha_M] + \Phi[\alpha_{yy}]$. For a given constituent material $\Phi[\alpha_M]$ is fixed. A null condition $\varepsilon = 0$ ($\Delta\Phi = 0, \pi, 2\pi\ldots$) can be generated at a desired λ_ε simply through engineering of the size of the circular nanoantenna, which controls both the spectral position and phase $\Phi[\alpha_{yy}]$ of the LPR[21]. As a result, measuring

λ_ε provides a precise and phase-sensitive detection of any shift of the LPR position (λ_ε and λ^* are not bound to be identical) induced by modifications of the dielectric properties of the near-field region local environment.

Bulk refractive index sensitivity. The magnetoplasmonic nanostructures investigated here are bottom-up, short-range-ordered nickel (Ni) cylindrical nanoantennas on glass (Fig. 2a)[25]. For determining S_{RI}, we measured the extinction spectra by immersing the samples in solutions with different indices of refraction n (Fig. 2b and Supplementary Fig. 1). The observed shift of λ^* leads to S_{RI} of 180 and 230 nm per refraction index unit (nm RIU^{-1}) for 30-nm-thick Ni nanoantennas with diameters of 100 and 160 nm, respectively (upper panels of Fig. 2b and Supplementary Fig. 1). In parallel, we determined the null-point wavelength λ_ε by measuring the spectral dependence of the polarization ellipticity variation $\Delta\varepsilon$ of the transmitted light, induced by applying and reversing the MO activation field H (Methods and Supplementary Fig. 2). The wavelength λ_ε is more precisely visualized by plotting the quantity $1/|\Delta\varepsilon|$, which resonates at λ_ε, as shown in the top panels of Figs 1b and 1c. Plotting the data in this manner makes it much easier to visualize the enormous gain in precision (limit of detection) and sensitivity of our approach. In addition, and for the sake of direct comparison with the FoM, which is conventionally utilized for defining the performances of a plasmonic detector, the plot of $1/|\Delta\varepsilon|$ provides the most sensible way to perform this comparison. We make it clear that comparison between sensitivity (both bulk and surface) and limit of detection performances of our approach with respect to plasmonic-based sensors are instead derived from direct measurements of $\Delta\varepsilon$ spectra and the precision (noise level) with which λ_ε is determined from such measurements.

The spectra of $1/|\Delta\varepsilon|$ for the two studied samples and for different values of n are shown in the lower panels of Fig. 2b and Supplementary Fig. 1. We observe that λ_ε undergoes a shift equal to that of λ^*, confirming the S_{RI} values determined above. It is clear that monitoring λ_ε instead of the extinction peak λ^* enables tracking of the resonance shift with an exceptionally higher precision.

In principle, our approach is characterized by a virtually unlimited value of the FoM since $1/|\Delta\varepsilon|$ is diverging at the resonant wavelength λ_ε. Practically, however, we can estimate a FWHM by accounting for experimental errors. Although polarization parameters can be determined with submicro-radiant resolution (down to 10 nrad), here we assume an experimental resolution of 5 micro-radians in the determination of $\Delta\varepsilon$, which is easily achievable without the utilization of advanced tools and/or fitting procedures, and consequently truncate the $1/|\Delta\varepsilon|$ spectra at 2×10^5 rad^{-1} (see the insets of the top panels of Figs 1b and 1c). We obtain a FWHM ranging

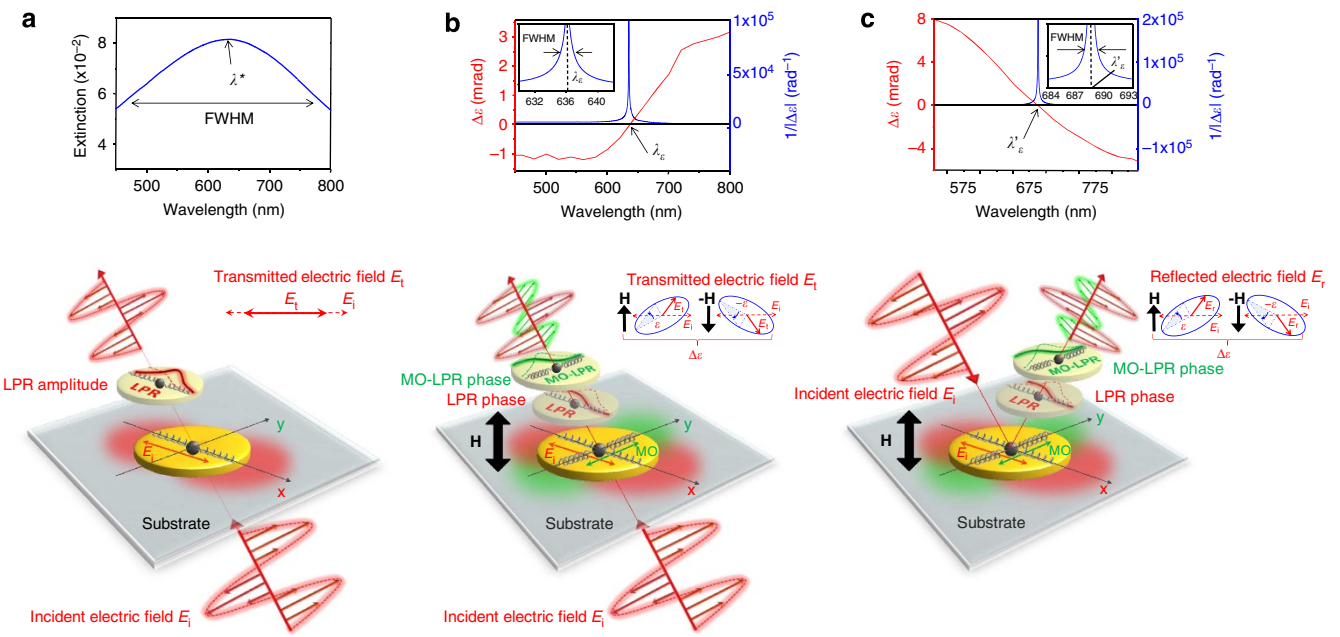

Figure 1 | LPR phase sensitivity in the transmitted light polarization. (**a**) When an incident light beam hits a ferromagnetic nanoantenna, the conduction electrons inside the nanostructure oscillate driven by the electric field E_i. These E_i-driven oscillations can be modelled as a damped spring-mass harmonic oscillator. A LPR is induced at a specific photon wavelength λ^*, yielding a peak in the extinction spectrum $(I_0-I_t)/I_0=1-(E_t/E_i)^2$, displayed in the top panel. (**b**) If the nanoantenna is magnetized perpendicularly to the surface plane, a MO-activity is turned on inducing a second MO-coupled LPR (MO-LPR) orthogonal to that directly driven by E_i. In a circular nanoantenna the MO-LPR resonates at the same λ^*. The simultaneous excitation of LPR and MO-LPR induces an elliptical polarization ε of the transmitted field E_t (refs 20,21). The null condition $\varepsilon=0$ is generated at a desired λ_ε (in general $\lambda_\varepsilon\neq\lambda^*$) simply through engineering of the size of the circular nanoantenna[21,34,35]. Measurement of λ_ε provides a precise phase-sensitive detection of the LPR position. The top panel displays typical $\Delta\varepsilon$ spectrum (red-line), as well as the $1/|\Delta\varepsilon|$ spectrum (blue-line) and its resonance at λ_ε. The close-up view of the $1/|\Delta\varepsilon|$ spectrum around λ_ε shown in the inset features a very narrow FWHM ($\sim$1.7 nm). (**c**) Similarly to the case described in **b**, the concerted action of the simultaneously excited LPR and MO-LPR can be exploited to actively manipulate the reflected light's polarization inducing the condition $\varepsilon=0$ at a desired λ'_ε. In general, $\lambda'_\varepsilon\neq\lambda_\varepsilon$ since in this case also the additional phase introduced by the substrate reflectivity contributes to the polarization of the reflected field E_r. As in transmission geometry, the detection of λ'_ε provides precise phase-sensitive detection of the LPR position. The top panel displays typical $\Delta\varepsilon$ spectrum (red line), as well as the $1/|\Delta\varepsilon|$ spectrum (blue line) and its resonance at λ'_ε. The close-up view of the $1/|\Delta\varepsilon|$ spectrum around λ'_ε shown in the inset features a very narrow FWHM (<1.7 nm). Both in transmission and reflection, the sensitivity increases further by measuring the magnetic field-induced variation $\Delta\varepsilon$ as ε reverses its sign upon inverting **H** (see Supplementary Fig. 2).

from 1.5 to 1.8 nm for the resonance of the $1/|\Delta\varepsilon|$ spectra (Fig. 2b and Supplementary Fig. 2). Taking the average FWHM of $\sim$1.7 nm means a FoM of more than 100 RIU^{-1} and approaching 150 RIU^{-1} for Ni nanoantennas with diameters of 100 and 160 nm, respectively. Such large FoM values greatly exceed even those for SPR in the same spectral range, which are often considered as theoretical limit references[10]. Figure 2c,d shows a comparison of the sensitivities of Au and Ni cylindrical nanoantennas on glass as well as their FoM, including that of SPR-based sensors.

The outstanding sensing performance of our magnetoplasmonic nanoantennas is better appreciated if compared directly with recently developed nanoplasmonic sensors. Improvements in FoM have been achieved by boosting the S_{RI} and/or reducing the FWHM of the LPR. S_{RI} enhancement has been realized by lifting metal nanostructures above substrates with dielectric pillars in order to expose more efficiently the surrounding environment to the LPR-enhanced electric field[26]. More efforts have been devoted to a reduction of the FWHM of LPRs caused by inherent losses in metallic nanostructures. The most effective approach relies on resonant coupling of LPRs with modes that possess a smaller FWHM. Such modes could, for example, be SPRs in an optically coupled thin metallic continuous layer[16], diffractive coupling among the nanostructures arranged in periodic arrays[15], and coherent coupling of different localized plasmon modes in nanostructures with complex shapes[9,17]. FoM values towards $\sim$60 have been reported upon resonant coupling of LPRs and SPRs[16]. More recently, a FoM value of up to 108 has been reported from periodic arrays of gold 'nano-mushrooms' that combine the two aforementioned approaches[10]. It is worth noting that all pathways towards enhancement of the FoM rely on a substantial increase in the complexity of the plasmonic nanostructures and arrangements design. In addition, the performance boost applies to a specific and narrow wavelength range where resonant coupling occurs. By exploiting the built-in phase sensitivity of the individual magnetoplasmonic nanoantennas, we circumvent the limitation due to their inherent losses, while keeping the nanostructuring process extremely simple and maintaining the outstanding performance over a broad spectral range.

Surface sensitivity. Applications to molecular detection rely on high sensitivity and FoM to the local variation of the index of refraction n. A reliable and precise assessment of the detection performance is an experimental challenge, as control of Δn on the molecular level is needed. The method of choice is the controlled deposition of extremely thin and removable films using molecular

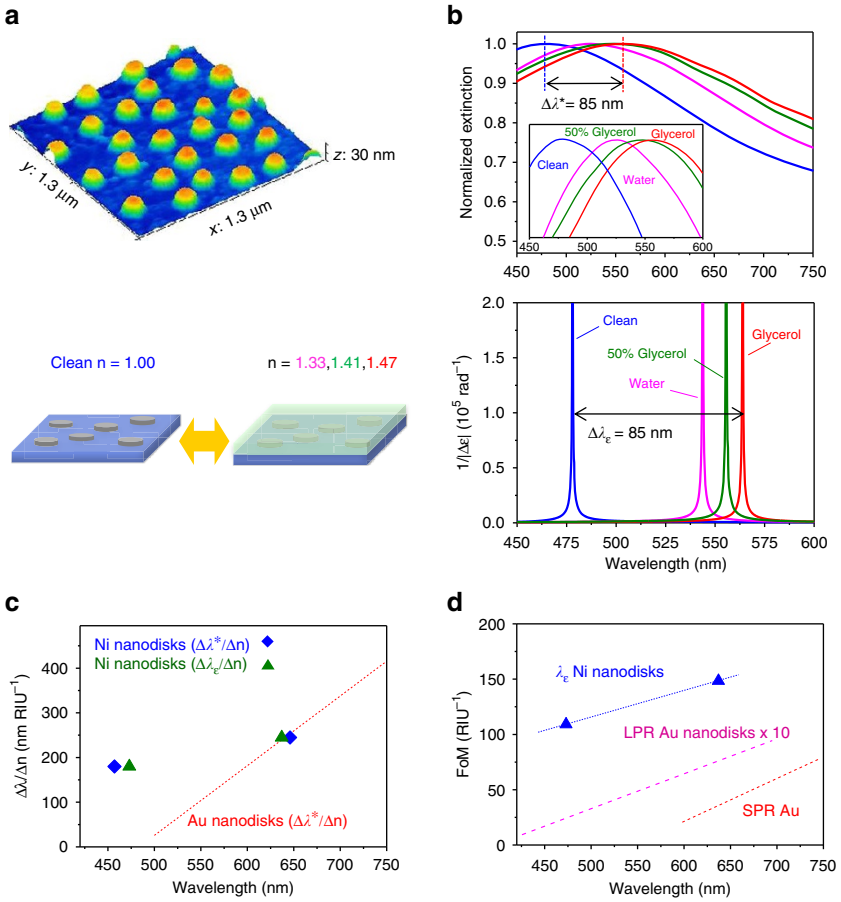

Figure 2 | Refractive index sensitivity of Ni magnetoplasmonic nanoantennas. (**a**) 3D AFM profile of Ni magnetoplasmonic nanoantennas on glass, with lateral dimensions of 103 ± 5 nm (diameter) and 30 ± 0.5 nm (thickness). (**b**; Top panel) extinction spectra of Ni cylindrical nanoantennas for different values of the embedding refractive index (clean $n=1$, water $n=1.33$, 50% Vol. glycerol $n=1.41$ and glycerol $n=1.47$; the inset shows a zoom of the resonance peaks in the spectral region 450–600 nm; bottom panel) plot of the inverse of transmitted light ellipticity variation $1/|\Delta\varepsilon|$ for the same values of the embedding refractive index as above. (**c**) Comparison between the bulk sensitivities of Au[26] ($\Delta\lambda^*/\Delta n$; red-dashed line) and Ni (both $\Delta\lambda^*/\Delta n$ and $\Delta\lambda_\varepsilon/\Delta n$; blue and green markers, respectively) cylindrical nanoantennas on glass. (**d**) Comparison between the bulk figure-of-merit of Au[26] [$(\Delta\lambda^*/\Delta n)$/FWHM] (purple dashed line) and Ni [$(\Delta\lambda_\varepsilon/\Delta n)$/FWHM] (blue markers are experimental data, blue dotted line is a guide for eyes) cylindrical nanoantennas, and Au surface plasmon resonance[14] (red dashed line), in the spectral range 420–750 nm.

layer deposition (MLD), an organic variant of atomic layer deposition[27,28]. The cyclic and self-terminating growth mechanisms of this method allow molecular-scale control of the polymer film growth and surface-dependent nucleation characteristics can be used for area-selective growth through matching of substrate and precursor chemistries. More importantly, MLD deposits polymer films from vapourized pure molecular fragments avoiding potentially negative impact of solvents (see also Methods).

For our experiments we used MLD of polyamide 6.6 (PA-6.6) with $n = 1.51$ (ref. 28). This polymer was chosen for convenience as the MLD process is well established and also, being a polyamide, it is representative for a large variety of polymers, peptides and proteins. In a first experiment, PA-6.6 was deposited 20 cycles at a time. The film thickness was measured by atomic force microscopy (AFM). The corresponding change of the local index of refraction was monitored by tracking λ_ε. Since the surface was modified only locally, we conducted polarization measurements also in reflection geometry as an alternative way to track λ_ε (see Fig. 1c). The experimental spectra and the resulting shift of λ_ε are shown in Fig. 3a,b. AFM images and their quantitative analysis show that PA-6.6 nucleated selectively on the Ni nanodisks and linearly grew up to ~100 cycles (Fig. 3c,d). Combining the two plots in Fig. 3b,d, we find S_{Surf} values of ~3 and ~5.3 in transmission and reflection geometry, respectively. The remarkable enhancement by a factor 1.7 of the S_{Surf} in reflection geometry, confirmed also by calculations, is a consequence of a larger shift of λ_ε caused by the additional phase contribution of uncovered substrate reflectivity (details in Supplementary Fig. 3). Such S_{Surf} value of ~5.3 is 3.5 times the surface sensitivity reported for Au-based SPR detectors in the same spectral region for the same refractive index[13]. Even more remarkable is the surface FoM (S_{Surf}/FWHM) of our magnetoplasmonic nanoantennas approach, whose value slightly larger than three is two orders of magnitude higher than the best surface FoM values achieved with plasmonic systems[14].

In order to demonstrate that very small quantities of material can be detected, PA-6.6 deposition, polarization ellipticity measurements and AFM characterization were performed sequentially for the very first cycles of MLD. Figure 4 shows that already after two MLD cycles an average increase in t of ~1.6 nm is determined by AFM. The resulting $\Delta\lambda_\varepsilon$ for the two measurement geometries confirm the surface sensitivities obtained in the previous experiment. On the basis of our very conservative error bar estimate in the measurement of $\Delta\varepsilon$, we can detect λ_ε with ~0.5 nm precision without the application of any fitting procedure (raw limit of detection).

Given the surface sensitivity (S_{Surf}) values ~3 and ~5.3 of our approach (transmission and reflection geometry, respectively), detection of subnanometre-thick PA-6.6 coverage, namely, a discontinuous monolayer (ML) of PA-6.6 on individual cylindrical Ni nanoantennas is achievable (~1.7 and ~1.0 Å for the two measurement geometries). A ML of PA-6.6 is ~8.5-Å thick[29], the precision above corresponds, in the case of transmission geometry, to a coverage of less than 0.2 ML, namely a ML covering less than 20% of the nanoantenna-exposed surface. The minimum detectable coverage reduces to 0.1 ML in reflection geometry. Such sub-ML coverage values are equivalent to PA-6.6 volumes of ~1,200 and 800 nm^3, that is, a remarkable mass sensitivity of ~1.2 and 0.8 ag per disk corresponding to

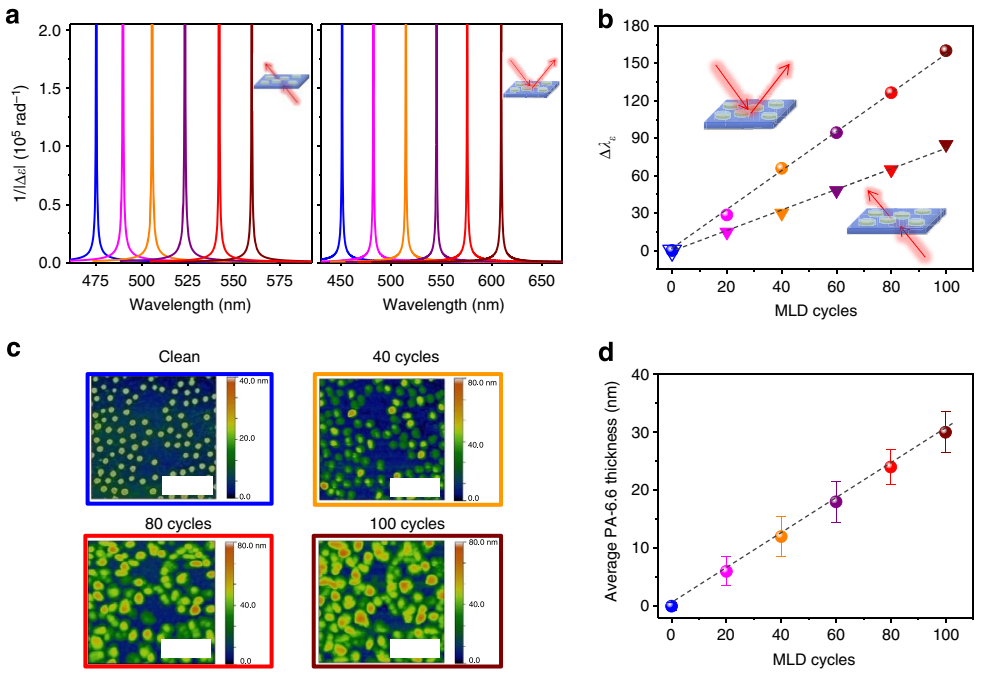

Figure 3 | Surface sensitivity assessment combining polarimetry and AFM measurements. (**a**) Plot of the inverse of the transmitted (left panel) and reflected (right panel) light ellipticity $1/|\Delta\varepsilon|$ spectra as a function of MLD cycles (at steps of 20 cycles). (**b**) $1/|\Delta\varepsilon|$ resonance wavelength λ_ε as a function of the MLD cycles for the two measurement geometries. In both cases, a linear dependence of λ_ε versus number of MLD cycles is observed (the black dashed lines are guide for eyes). The shift of λ_ε saturates for a number of MLD cycles equal to 120, corresponding to a PA-6.6 thickness of ~35 nm, as shown in Supplementary Fig. 7 for transmission geometry case. Such PA-6.6 thickness agrees well with the near-field spatial extension (see Supplementary Fig. 4). (**c**) AFM images taken from the same sample region (total area imaged 2.7 × 2.7 μm^2) after different numbers of MLD cycles. The AFM images show that PA-6.6 grows only on top of the nanoantennas. The colours of the frames refer to the corresponding coloured polarimetry (**b**) and thickness (**d**) data points. The length of the white scale bars in the images corresponds to 1 μm. (**d**) PA-6.6 average thickness as function of the MLD cycles after AFM topography image analysis. Surface sensitivities (spectral variation of λ_ε divided by the average nylon thickness) of ~3 (transmission) and ~5.3 (reflection) are found combining plots (**b**,**d**). The error bars indicate the s.d. from the average thicknesses measured analysing the AFM images.

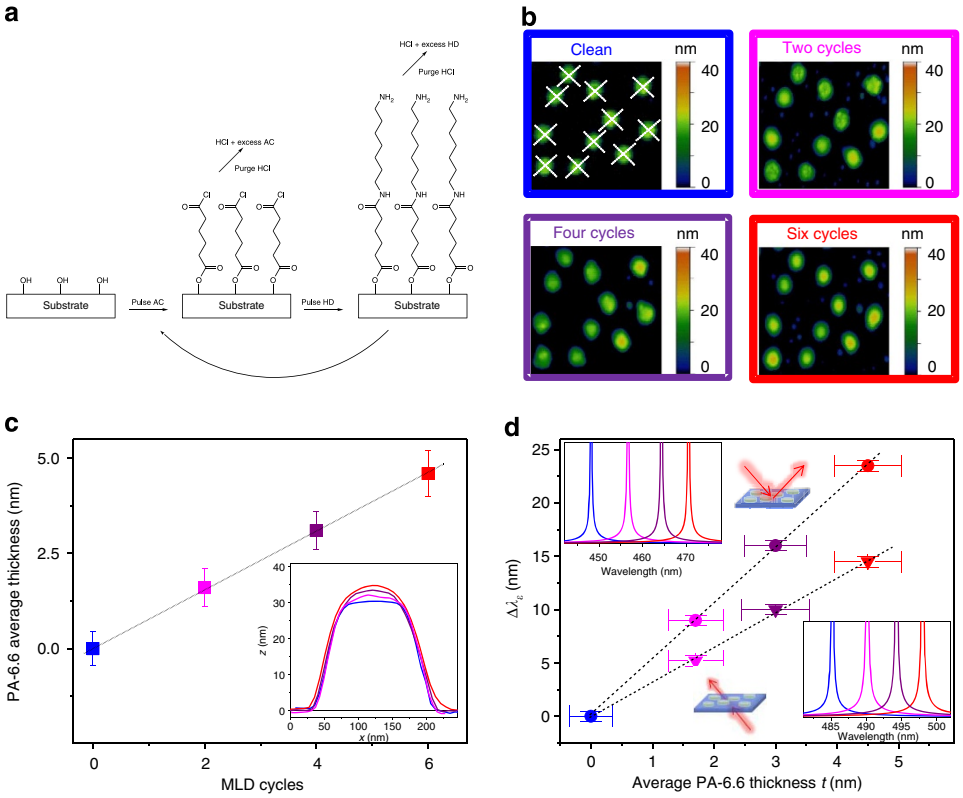

Figure 4 | Surface sensitivity in the first few cycles of PA-6.6 MLD. (**a**) Schematic of one cycle of the MLD process for PA-6.6. A substrate with –OH surface groups is exposed to a pulse of AC. The AC reacts with these –OH groups creating the by-product HCl, which is purged away along with any unreacted AC. Next, a pulse of HD is introduced to the reaction chamber and reacts with the available –Cl groups. Again, the by-product is HCl, which is purged away along with any unreacted HD. This process is repeated until the desired thickness is achieved. Nominally, the process has a growth rate of ~0.8 nm per cycle[29]. (**b**) AFM images taken from the same sample region (total area imaged $1.2 \times 1.2\,\mu m^2$) before and after PA-6.6 MLD. The colours of the frames refer to the corresponding coloured thickness (**c**) and polarimetry (**d**) data points. (**c**) PA-6.6 average thickness as function of the MLD cycles after AFM topography image analysis. The error bars indicate the s.d. from the average thicknesses shown in the inset, which shows the line profiles of all the disks included in the images in **b**. The line profiles are taken along two orthogonal directions, which are shown as white dashed lines only in the AFM image of the clean sample in **b**. (**d**) Plot of the inverse of transmitted and reflected light ellipticity λ_ε as a function of MLD cycles (black dashed lines are guide for eyes). Surface sensitivities of ~3.1 (transmission) and ~5.4 (reflection) are found combining plots (**c**,**d**), in excellent agreement with the results presented in Fig. 3. The horizontal error bars indicate the s.d. from the average thicknesses shown in the inset in (**c**). The vertical error bars indicate the experimental error in the magneto-optical measurements. The insets show the corresponding $1/|\Delta\varepsilon|$ spectra for the two measurement geometries (reflection—top-left inset and transmission—bottom-right inset).

~3,300 and 2,200 molecules of PA-6.6 per disk (density of amorphous PA-6.6 is $1.05\,g\,cm^{-3}$ and its molecular weight is $226\,g\,mol^{-1}$). Such minimum detectable coverage is based on extrapolation and assumes that the electric near field is uniformly distributed in the vicinity of the Ni nanoantenna surface exposed to the environment, that is, the surface sensitivity is not, or weakly, space-dependent. This condition is fulfilled to a good extent for our nanodisks with a diameter of 100 nm as we verified by the simulations of the near field produced by the excitation of a LPR performed using Lumerical (see Supplementary Fig. 4). A raw limit of detection of a few zg per nanoantenna can be achieved considering the submicro-radiant resolution of advanced polarimetry tools.

These sensing performances could be further improved by applying the same strategies as employed for noble metal nanoplasmonic systems for label-free detection, such as lifting of the nanostructures from the substrate and exploiting resonant coupling between LPRs to modes with narrow FWHM.

In addition, reducing the diameter of the cylindrical Ni nanoantennas would improve the limit of detection, since the surface sensitivity is weakly dependent on the diameter and, consequently, also the ability to detect a ML coverage of 20 and 10% of the nanoantenna-exposed surface, which for smaller nanoantennas corresponds to proportionally smaller volumes of material.

So far, the limit of detection of our approach was derived based on the signal-to-noise ratio of the measurements, without any mathematical fit of the data, and compared with those of similar 'raw' estimates of sensitivity based on absorption spectrum measurement. This comparison demonstrates the radically improved sensitivity enabled by our nanomagnetoplasmonic approach with respect to plasmon-based sensors.

Higher sensitivity and limit of detection values are reported in literature for plasmon-based sensors, which are achieved by application of fitting procedures[30,31]. We mention here that the application of fitting procedures of our data confirms the higher sensitivity of our approach as shown in the Supplementary Fig. 5. Indeed, a mass sensitivity in the sub-zg per nanoantenna, down to a few yg per nanoantenna, can be achieved through the application of fitting procedures opening a pathway to mass sensitivity corresponding to ~10 molecules of PA-6.6 per disk (or, equivalently, of any material having $n \sim 1.5$ and a density of $\sim 1\,g\,cm^{-3}$, which is the case of many polymers and biomolecules).

Discussion

Magnetoplasmonic nanoantennas that support magneto-optically induced localized plasmon resonances have been synthesized in order to induce a null condition of the transmitted/reflected light polarization ellipticity at desired wavelengths. The obtained null condition allows for an easily measurable and extremely precise phase-sensitive detection of localized plasmon resonances. Such magnetoplasmonic nanoantennas can be used for optical sensing of local refractive index variations with enhanced sensitivity and unrivalled values for the FoM, even exceeding the theoretically predicted upper limit for sensing based on propagating SPRs. Our approach requires extremely simple and scalable nanostructuring processes and offers a remarkably improved sensitivity performance in a large spectral range. To conclude, we would like to emphasize that the ultrasensitive sensing capabilities of our magnetoplasmonic nanoantennas can be used also in nanoplasmonic biosensing (for instance, cancer serum detection). Ni surfaces are covered by an ultrathin layer of oxidized Ni. Such surfaces can be functionalized with either silanes or even better with Histidin tags (His6)[32] on par with Au surface functionalization with thiolate chemistry, thus informing our selected Ni as the material for our nanoantennas. As an alternative, one could even deposit a thin layer of Au, which will not affect the plasmonic behaviour (even improve it, according to literature), and use conventional thiolate chemistry. In addition to biosensing, there are also many other potential civil and/or military applications that do not require surface functionalization and would enormously benefit from our approach like chemical sensing of toxic materials, explosives and ultra-precise thickness-monitoring applications.

Methods

Optical and MO measurements. The extinction spectra $(I_0 - I_t)/I_0$, where I_0 and I_t are the intensities of the incident and transmitted light, respectively, were taken in the wavelength range 420–900 nm. The intensity of the light passing through the substrate without nanostructures on top was taken as the reference I_0 signal.

The wavelength dependence of the magneto-optically induced ellipticity change $\Delta\varepsilon$ of the transmitted or reflected light was measured using MO Faraday (incidence angle 0°) and Kerr (incidence angle 2.5°) effect spectrometers working in polar geometry in the wavelength range 420–950 nm. The incident light beam was linearly polarized with either p- or s-polarization. $\Delta\varepsilon$ was measured by switching the polarity of a magnetic field $H = 4$ kOe applied normal to the sample plane to activate the MO coupling in the nanoantennas' constituent material. As shown schematically in Supplementary Fig. 2, in the polar-Kerr geometry $\Delta\varepsilon$ was measured at each wavelength with the transmitted beam passing through a photoelastic phase modulator and a polarizer before detection. A lock-in amplifier was used to filter the signal at the modulation frequency in order to retrieve $\Delta\varepsilon$ (ref. 33). Our experimental set-up allows measuring polarization parameters, like ε and $\Delta\varepsilon$, with submicro-radiant precision, although in our analysis of the measured spectra we assumed a 5 micro-radians error bar, for the sake of demonstrating that our approach guarantees a high sensitivity even using extremely simple measurement set-ups as that shown in the Supplementary Fig. 6. It is worth mentioning that $\Delta\varepsilon$ can be equivalently measured in reflection geometry with the light impinging on either magnetoplasmonic sample surface side (Fig. 1c). Measurement of $\Delta\varepsilon$ with the light beam impinging from the glass bottom surface can be particularly appealing for implementation of our approach in practical devices (Supplementary Fig. 6).

Sensing experiments. Bulk sensitivity experiments were performed in a microfluidic cell where different liquids, with different refractive index, were injected every time. We used liquids and mixtures whose refractive indexes are well known, namely water ($n = 1.33$), glycerol ($n = 1.47$) and 50% glycerol volume in water ($n = 1.41$).

For surface sensitivity assessment, MLD of polyamide 6.6 (PA-6.6) was carried out in a commercially available Cambridge Nanotech/Ultratech Savannah system using alternating pulses of adipoyl chloride (AC; Sigma Aldrich) and 1,6-hexamethylenediamine (HD; Sigma Aldrich) with the following pulse/purge/pulse/purge parameters; 0.5 s/30 s/0.5 s/30 s. The AC and HD were heated to 70 and 80 °C, respectively. The reaction chamber was maintained at 85 °C throughout the reaction. Before deposition the samples were treated using 5-min cycles of acetone and isopropanol ultrasonication, and then exposed to Ar plasma at 90 W for 60 s to eliminate residues of organic materials. Coating and cleaning procedures were repeated several times to ensure the reproducibility of the experiment (both polarization and thickness of PA-6.6 deposits). The thickness of the PA-6.6 deposits was monitored via AFM. The AFM measurements were carried out in the same region after each MLD cycles and MOKE measurement step, using an Agilent 5500 AFM microscope with a Si tip operated in tapping mode. The images were analysed using the Gwyddion software package in order to extract the average thickness values of PA-6.6 deposits.

Both bulk and surface sensitivity experiments were repeated five times each, giving the same results within the experimental errors reported above.

Sample fabrication. Bottom-up hole mask colloidal lithography was used to pattern the Ni nanodisks[25]. The following process steps were applied in all presented examples. The substrates used are $10 \times 10 \times 1$ mm^3 pieces of microscope slide glass (VWR International). The glass substrates were first cleaned through 5-min cycles of acetone, isopropanol and water ultrasonication. A poly(methyl methacrylate) (PMMA) film (2 wt % PMMA diluted in anisole, MW = 950,000) was spin-coated on a clean surface and followed bysoft baking (170 °C, 10 min on a hot plate). Reactive oxygen plasma treatment (50 W, 5 s, 250 mTorr, Plasma Therm Batchtop RIE 95 m) was applied in order to decrease the polymer film hydrophobicity and avoid spontaneous de-wetting of the surface during subsequent polyelectrolyte and particle deposition steps, which would introduce inhomogenities in the particle distribution. Providing a net charge to the PMMA surface by pipetting a solution containing a positively charged polyelectrolyte on the film (polydiallyldimethylammonium MW 200,000–350,000, Sigma Aldrich, 0.2 wt % in Milli-Q water, Millipore), followed by careful rinsing with de-ionized water in order to remove excess polydiallyldimethylammonium and blow-drying with a N_2 stream. Deposition of a water suspension containing negatively charged polystyrene particles (sulfate latex, Invitrogen, 0.2 wt % in Mili-Q water) and N_2 drying in a similar manner as described above, leaving the PMMA surface covered with uniformly distributed PS-spheres. Evaporation of an oxygen plasma-resistant thin film of Au. Removing the PS spheres using tape stripping (SWT-10 tape, Nitto Scandinavia AB), resulting in a mask with holes arranged in a pattern determined by the self-assembled colloidal particles. Transfer of the hole-mask pattern into the sacrificial layer via an oxygen plasma treatment (50 W, 250 mTorr, Plasma Therm Batchtop RIE 95 m), which effectively removes all PMMA situated underneath the holes in the film, leaving the surface covered with a thin-film mask supported on a perforated, undercut polymer film. Ni deposition is carried out by e-beam-assisted evaporation (AVACHVC600). Lift off was carried out using acetone at room temperature or 50 °C for 5–10 min. The filling factor (surface covered by Ni nanoantennas normalized to area of the sample surface) can be varied between 5 and 30% in a controlled manner. The filling factor of the samples utilized in our experiments can be estimated to be around 15%.

References

1. Sandtke, M. & Kuipers, L. Slow guided surface plasmons at telecom frequencies. *Nat. Photon.* **1,** 573–576 (2007).
2. Ferry, V. E., Sweatlock, L. A., Pacifici, D. & Atwater, H. A. Plasmonic nanostructure design for efficient light coupling into solar cells. *Nano Lett.* **8,** 4391–4397 (2008).
3. Cui, Y., Wei, Q. Q., Park, H. K. & Lieber, C. M. Nanowire nanosensors for highly sensitive and selective detection of biological and chemical species. *Science* **293,** 1289–1292 (2001).
4. Anker, J. N. *et al.* Biosensing with plasmonic nanosensors. *Nat. Mater.* **7,** 442–453 (2008).
5. Stewart, M. E. *et al.* Nanostructured plasmonic sensors. *Chem. Rev.* **108,** 494–521 (2008).
6. Larsson, E. M., Syrenova, S. & Langhammer, C. Nanoplasmonic sensing for nanomaterials science. *Nanophotonics* **1,** 249–266 (2012).
7. Mayer, K. M. & Hafner, J. H. Localized surface plasmon resonance sensors. *Chem. Rev.* **111,** 3828–3857 (2011).
8. Chung, T., Lee, S. Y., Song, E. Y., Chun, H. & Lee, B. Plasmonic nanostructures for nano-scale bio-sensing. *Sensors* **11,** 10907–10929 (2011).
9. Kravets, V. G. *et al.* Singular phase nano-optics in plasmonic metamaterials for label-free single-molecule detection. *Nat. Mater.* **12,** 304–309 (2013).
10. Shen, Y. *et al.* Plasmonic gold mashroom arrays with refractive index sensing figures of merit approaching the theoretical limit. *Nat. Commun.* **4,** 2381 (2013).
11. Aćimović, S. S. *et al.* LSPR chip for parallel, rapid, and sensitive detection of cancer markers in Serum. *Nano Lett.* **14,** 2636–2641 (2014).
12. Kabashin, A. V. *et al.* Plasmonic nanorod metamaterials for biosensing. *Nat. Mater.* **8,** 867–871 (2009).
13. Svedendahl, M., Chen, S., Dmitriev, A. & Käll, M. Refractometric sensing using propagating versus localized surface plasmons: a direct comparison. *Nano Lett.* **9,** 4428–4433 (2009).
14. Otte, M. A. *et al.* Identification of the optimal spectral region for plasmonic and nanoplasmonic sensing. *ACS Nano* **4,** 349–357 (2010).
15. Offermans, P. *et al.* Universal scaling of the figure of merit of plasmonic sensors. *ACS Nano* **5,** 5151–5157 (2011).
16. Lodewijks, K. *et al.* Tuning the Fano resonance between localized and propagating surface plasmon resonances for refractive index sensing applications. *Plasmonics* **8,** 1379–1385 (2013).

17. Verellen, N. *et al.* Plasmon line shaping using nanocrosses for high sensitivity localized surface Plasmon resonance sensing. *Nano Lett.* **11,** 391–397 (2011).
18. Lodewijks, K., Van Roy, W., Borghs, G., Lagae, L. & Van Dorpe, P. Boosting the Figure-Of-Merit of LSPR-based refractive index sensing by phase-sensitive measurements. *Nano Lett.* **12,** 1655–1659 (2012).
19. Chen, J. *et al.* Plasmonic nickel nanoantennas. *Small.* **7,** 2341–2347 (2011).
20. Bonanni, V. *et al.* Designer magnetoplasmonics with nickel nanoferromagnets. *Nano Lett.* **11,** 5333–5338 (2011).
21. Maccaferri, N. *et al.* Tuning the magneto-optical response of nanosize ferromagnetic Ni disks using the phase of localized plasmons. *Phys. Rev. Lett.* **111,** 167401 (2013).
22. Belotelov, V. I. *et al.* Enhanced magneto-optical effects in magnetoplasmonic crystals. *Nat. Nanotech.* **6,** 370–376 (2011).
23. Armelles, G., Cebollada, A., García-Martín, A. & González, M. U. Magnetoplasmonics: combining magnetic and plasmonic functionalities *Adv. Opt. Mater.* **1,** 10–35 (2013).
24. Lodewijks, K. *et al.* Magnetoplasmonic design rules for active magneto-optics. *Nano Lett.* **14,** 7207–7214 (2014).
25. Fredriksson, H. *et al.* Hole-Mask Colloidal Lithography. *Adv. Mater.* **19,** 4297–4302 (2007).
26. Dmitriev, A. *et al.* Enhanced nanoplasmonic optical sensors with reduced substrate effect. *Nano Lett.* **8,** 3893–3898 (2008).
27. Knez, M., Nielsch, K. & Niinistö, L. Synthesis and surface engineering of complex nanostructures by atomic layer deposition. *Adv. Mater.* **19,** 3425–3438 (2007).
28. George, S. M. Atomic layer deposition: An overview. *Chem. Rev.* **110,** 111–131 (2010).
29. Du, Y. & George, S. M. Molecular layer deposition of nylon 66 films examined using in situ FTIR spectroscopy. *J. Phys. Chem. C* **111,** 8509–8517 (2007).
30. Dahlin, A. B., Tegenfeldt, J. O. & Höök, F. Improving the instrumental resolution of sensors based on localized surface plasmon resonance. *Anal. Chem.* **78,** 4416–4423 (2006).
31. Chen, S., Svedendahl, M., Käll, M., Gunnarsson, L. & Dmitriev, A. Ultrahigh sensitivity made simple: nanoplasmonic label-free biosensing with an extremely low limit-of-detection for bacterial and cancer diagnostics. *Nanotechnology* **20,** 434015 (2009).
32. Hochuli, E., Bannwarth, W., Döbeli, H., Gentz, R. & Stüber, D. Genetic Approach to Facilitate Purification of Recombinant Proteins with a Novel Metal Chelate Adsorbent. *Nat. Biotechnol.* **6,** 1321–1325 (1988).
33. Vavassori, P. Polarization modulation technique for magneto-optical quantitative vector magnetometry. *Appl. Phys. Lett.* **77,** 1605–1607 (2000).
34. Maccaferri, N. *et al.* Polarizability and magnetoplasmonic properties of magnetic general nanoellipsoids. *Opt. Express* **21,** 9875–9889 (2013).
35. Maccaferri, N. *et al.* Effects of a non-absorbing substrate on the magneto-optical Kerr response of plasmonic ferromagnetic nanodisks. *Phys. Status Solidi A* **211,** 1067–1075 (2014).

Acknowledgements

P.V., N.M., K.E.G. and M.Kn. acknowledge financial support from the Basque Government (Programs No. PI2012-47 and PI2013-56) and the Spanish Ministry of Economy and Competitiveness (Projects No. MAT2012-36844 and MAT2012-38161). N.M. acknowledges support from the Doctoral Programme of the Department of Education, Linguistic Policy and Culture of the Basque Government (Grant No. PRE_2013_1_975). P.V. and N.M. also thank Paolo Biagioni for support on simulations using Lumerical FDTD Solutions Software. T.V.A.G.d.O. acknowledges support from the European Research Council (Grant No. 257654-SPINTROS). Z.P., A.D. and J.Å. acknowledge the Swedish Research Council (VR) and the Swedish Foundation for Strategic Research, SSF (Z.P. and A.D.: Framework programme Functional Electro-magnetic Metamaterials, Project No. RMA08; J.Å.: Successful Research Leader Program). M.K. and S.v.D. acknowledge support from the National Doctoral Programme in Nanoscience and the Academy of Finland (Grant No. 263510).

Author contributions

P.V. conceived the experiments. N.M. performed optical and magneto-optical measurements and FDTD simulations. K.E.G. and M.Kn. performed molecular layer deposition. T.V.A.G.d.O. performed AFM measurements and developed non-destructive sample cleaning procedures. M.K. and S.v.D. contributed to the measurements and data analysis. Z.P. and A.D. fabricated the samples. N.M. and P.V. analysed the data and all authors wrote the manuscript.

Additional information

Supplementary Information accompanies this paper at http://www.nature.com/naturecommunications

Competing financial interests: The authors declare no competing financial interests.

Reprints and permission information is available online at http://npg.nature.com/reprintsandpermissions/

How to cite this article: Maccaferri, N. *et al.* Ultrasensitive and label-free molecular-level detection enabled by light phase control in magnetoplasmonic nanoantennas. *Nat. Commun.* 6:6150 doi: 10.1038/ncomms7150 (2015).

nature COMMUNICATIONS

DOI: 10.1038/ncomms8431

Corrigendum: Ultrasensitive and label-free molecular-level detection enabled by light phase control in magnetoplasmonic nanoantennas

Nicolò Maccaferri, Keith E. Gregorczyk, Thales V.A.G. de Oliveira, Mikko Kataja, Sebastiaan van Dijken, Zhaleh Pirzadeh, Alexandre Dmitriev, Johan Åkerman, Mato Knez & Paolo Vavassori

Nature Communications 6:6150 doi: 10.1038/ncomms7150 (2015). Published 2 Feb 2015; Updated 18 Jun 2015

This Article contains typographical errors in the equations of the last sentence of the first paragraph of the Results section. This sentence should read 'In the present case, the spin–orbit transversally induced dipole is given by $p_y = \alpha_{yx}E_x^0 = \left[\varepsilon_{yx}\alpha_{yy}\alpha_{xx}/(\varepsilon_0 - \varepsilon_m)^2\right]E_x^0$ (considering the circular shape of our nanoantennas, $\alpha_{yy} = \alpha_{xx}$, that is, the two LPRs resonate at the same wavelength, and the expression above can be simplified to $p_y = \alpha_{yx}E_x^0 = \left[\varepsilon_{yx}\alpha_{xx}^2/(\varepsilon_0 - \varepsilon_m)^2\right]E_x^0$).'